Microstructure reconstruction and homogenization of porous Ni-YSZ composites for temperature dependent properties

S.A. Tabei [a], A. Sheidaei [b], M. Baniassadi [c], F. Pourboghrat [b], H. Garmestani [d,*]

[a] G. W. Woodruff School of Mechanical Engineering, Georgia Institute of Technology, 801 Ferst Drive NW, Atlanta, GA 30332, USA
[b] Department of Mechanical Engineering, Michigan State University, 428 S. Shaw Lane, East Lansing, MI 48824, USA
[c] University of Strasbourg, IMFS, 2 Rue Boussingault, 67000 Strasbourg, France
[d] School of Materials Science and Engineering, Georgia Institute of Technology, 771 Ferst Drive NW, Atlanta, GA 30332, USA

HIGHLIGHTS

► We reconstructed a porous Ni–YSZ microstructure.
► Elastic properties of the realized sample are computed.
► Elastic response in shear and tension are different in terms of anisotropy.
► Thermal properties as functions of temperature are also computed.

ARTICLE INFO

ABSTRACT

In this work, a 3D microstructure of a porous Ni–YSZ composite is reconstructed using a recently developed Monte Carlo methodology. The 3D reconstruction starts by analyzing 2D SEM micrographs of real composite materials, which yield initial nucleation sites for different phases. The so-called cellular automaton algorithm, which is observed in insect colonies and bacteria growth in nature, controls growth kinetics of the initial nuclei. After successful growth and completion of the reconstruction process, FEM simulations are applied to characterize elastic and thermal properties of the reconstructed material. A porous Ni–YSZ composite reconstructed by this method shows mechanical behavior in between full isotropic and full orthotropic with an average Young's moduli of 17 GPa at room temperature and 10.2 GPa at 1000 °C, which are consistent with experimentally reported values. The variation in effective shear and Poisson's moduli as a function of temperature is also studied. Thermal conductivity and thermal expansion coefficient of the digital material are derived as functions of temperature; revealing a relatively isotropic property in thermal conductivity and an increase in anisotropy in thermal expansion coefficient by increasing temperature.

1. Introduction

Continuously growing energy prices and exhausting fossil fuel resources, in addition to environmental factors, strictly demand for more efficient energy sources. In this regard, intense research has been conducted in order to replace fossil fuel energy with more efficient, cleaner energy resources. One promising technology is the fuel cell [1], which has stimulated a great deal of attention due to its better compatibility with modern needs of an energy resource in terms of economy, efficiency and cleanliness compared to traditional sources of energy. A fuel cell is a device that converts chemical energy into electricity by means of conducting an electrochemical reaction between the fuel (usually hydrogen or light hydrocarbons) and oxygen instead of a direct combustion. Several types of fuel cells, such as solid oxide fuel cell, phosphoric acid fuel cell, alkaline fuel cell, molten carbonate fuel cell and etc., have been developed and deeply studied. Solid oxide fuel cells (SOFC) have several advantages over other types including utilizing a solid material as the electrolyte which avoids corrosive liquid electrolytes, yielding one of the highest efficiencies amongst all fuel cell types [2,3] without requiring noble precious metals in anode/cathode parts, flexibility in choice of fuel and so forth [2–5]. However, one of the major drawbacks of SOFCs is that their working

* Corresponding author.
E-mail addresses: tabei@gatech.edu (S.A. Tabei), sheidaei@egr.msu.edu (A. Sheidaei), majid.baniassadi@imfs.u-strasbg.fr (M. Baniassadi), pourbogh@egr.msu.edu (F. Pourboghrat), hamid.garmestani@mse.gatech.edu (H. Garmestani).

temperature is usually above 600 °C as a result of low ionic conductivities of commercially available solid electrolytes at lower temperatures. Although having the reaction products at high temperatures can be beneficial in few cases [3], it is usually considered a drawback since working at elevated temperatures dramatically increases the risk of material failure due to thermal expansion mismatch between different parts of the fuel cell. In addition, at higher temperatures, the mechanical strength of commercial SOFC materials drops, which leads to more susceptibility to mechanical failure.

Yittria-stabilzed Zirconia (Y_2O_3–ZrO_2 or YSZ) is one of the top candidates for SOFC electrolytes due to a combination of comparatively high ionic conductivity, high mechanical strength and high thermal conductivity at operation temperatures of the fuel cell [6–8]. The anode composite necessarily needs to be porous since the fuel, which is in the form of a gas or a gas mixture, must be able to pass through the anode and reach the electrolyte in order to complete the electrochemical reactions. Amongst many candidates for the anode [8–10], porous Ni–YSZ composites have attracted a great deal of attention. These composites provide the least thermal expansion mismatch between anode and electrolyte and, on the condition of full percolation of the nickel phase, provide excellent electrical conductivity. In addition, high-temperature elastic properties and high thermal conductivity of porous Ni–YSZ composites are within the desired range [2,9–12].

Microstructure is one of the most essential factors that govern electrical, mechanical and thermal response of a composite. Volume fraction, phase distribution, average aggregate size, morphology and percolation of each phase significantly affect the properties. In addition, presence of any gradient in aggregate size, as well as textures in crystalline phases, can dramatically alter the properties. Accordingly, for the case of porous Ni–YSZ composites, a wide range of reported values in properties can be found. For example, ~20–80 GPa ranges for effective Young's modulus [13–15] at room temperature; 10–60 W mK^{-1} for effective thermal conductivity [16] and 1×10^{-6} to 20×10^{-6} for thermal expansion coefficient [16,17] are reported. The fact that working temperatures of SOFCs are well above room temperature stimulates direct measurement or computation of essential properties of SOFCs materials as functions of temperature.

Although 2D images provide valuable information in studying the microstructure, for complete understating of microstructure–property relations, 3D representations are pursued [18]. Experimental techniques of 3D imaging are usually costly and limited to the resolution of the used tools. Therefore, computer aided methods have been developed to realize 3D microstructures [19–21]. These methods can use different experimental information as inputs to build the digital microstructure. Direct measurement of all important properties of SOFCs at their wide range of working temperatures is a laborious process. Therefore, 3D reconstruction, in addition to applying computer simulations to estimate the properties alongside experiments, appears reasonable. In order to determine the desired properties, first, the heterogeneous digital microstructure must be built and introduced to the computer. Second, a homogenization technique must be applied to obtain the materials properties.

In this work, we first computationally realized a microstructure of a porous Ni–YSZ composite by using SEM images (Fig. 1) of a real sample with 8 mol% of Y_2O_3 doped into $ZrO2$ structure (8YSZ). This realization technique is based on a modified Monte Carlo simulation that has been recently reported to successfully yield the 3D microstructure of composites [20,21]. Then, we reassured statistical equivalence of the digital microstructure to real samples. Afterward, by finite element simulations, we computed the properties as functions of temperature.
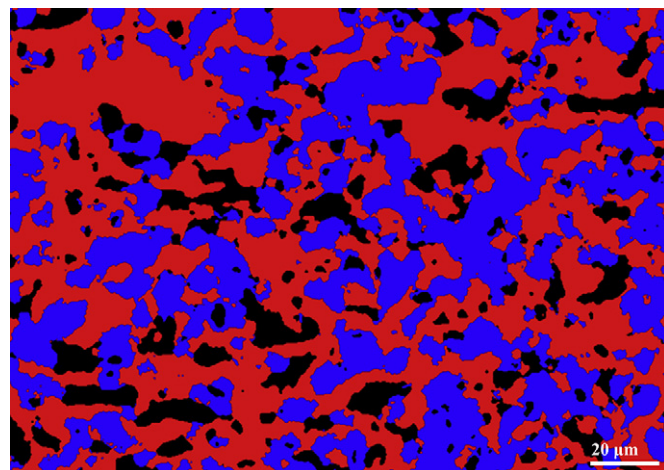

Fig. 1. SEM image of a real porous Ni–YSZ sample. The image is taken with the backscattered electron detector and phases are colored for more clarity. Red, blue and black represent YSZ, Ni and voids respectively [20]. (For interpretation of the references to color in this figure legend, the reader is referred to the web version of this article.)

2. Methodology

2.1. 3D reconstruction

For any heterogeneous microstructure with the total volume V_{tot}, the volume fraction of phase i, v_i, is defined as follows:

$$v_i = \frac{V_i}{V_{tot}} \tag{1}$$

where V_i is the total volume of phase i. Obviously:

$$\sum_{i=1}^{n} v_i = 1 \tag{2}$$

where n is the total number of phases.

Now, if N random points are thrown in the microstructure a sufficiently large number of times; P_i, defined as the probability of the points falling into a specific phase, e.g. phase i, is simply the volume fraction of phase i as shown in Eq. (3). This is a statistical probability function which is called the "one-point correlation" function.

$$P_i^1 = \left. \frac{N_i}{N} \right|_{N \to \infty} = v_i \tag{3}$$

where N_i is the number of points falling in phase i. The superscript 1 in P denotes the order of the probability for the "one"-point correlation function. The next correlation function that is widely used in statistical representation of a material is the two-point correlation function. If we randomly throw N vectors with length r into the microstructure a sufficiently large number of times, the probability that both ends of the fall on specific phases i and j is called the two-point correlation function, as represented by Eq. (4):

$$P_{ij}^2(\bar{r}) = \left. \frac{N_{ij}}{N} \right|_{N \to \infty}, \quad \bar{r} = |r_j - r_i|, r_i \in i \text{ and } r_j \in j \tag{4}$$

where r_i and r_j are vectors ending in phases i and j respectively. It can be shown that at zero length, the two-point correlation

function reduces to P_i^1, and at large lengths, it asymptotically reduces to $v_i v_j$ [22]. Therefore, it can provide more information on microstructure compared to the one-point correlation function. Considering the normalization properties of the correlation functions, one can prove that two restrictions are imposed on correlation functions. First, summation of all possible cases of probability functions should add up to unity (i.e. $\sum_i \sum_j P_{ij}^2(\bar{r}) = 1$). Second, probability functions are symmetric (i.e. P_{ij} P_{ji} [22]). These two conditions limit the number of independent two-point correlation functions. Hence, for a two-phase composite, there are two independent two-point correlation function (e.g. P_{11} and P_{12}), and for a three-phase composite, there are three independent two-point correlation functions (e.g., P_{11}, P_{12}, and P_{22}).

The linkage between two-point statistical functions and microstructure of materials originates from x-ray diffraction [23]. As a result of this connection, the two-point correlation function (known as pair correlations in scattering theory) has been extensively applied to describe microstructures [22]. In this work, we used the two-point correlation functions as means of comparing the reconstructed sample to real material.

The applied reconstruction technique is composed of two parts: (a) 2D reconstruction and (b) 3D reconstruction. Each part consists of three steps: (i) cell generation, (ii) cell redistribution and (iii) cell growth. In each step, there are several parameters that need to be optimized to secure a final microstructure which is statistically identical to the real material. Building a 2D microstructure before the final real 3D microstructure is essential since the optimized algorithm parameters of the 2D microstructure are used as initial values for the 3D reconstruction. Otherwise, starting directly from a 3D pattern by random initial values prolongs the procedure and jeopardizes the convergence of the model if initial values had not been suitably chosen.

For either 2D or 3D reconstruction, the three steps are repeated until an objective function (OF) is minimized. Eq. (5) displays the objective function used in our technique:

$$OF = \left(P_{11,real}^2 - P_{11,sim}^2\right)^2 + \left(P_{12,real}^2 - P_{12,sim}^2\right)^2$$
$$+ \left(P_{22,real}^2 - P_{22,sim}^2\right)^2 \tag{5}$$

where $P_{ij,real}^2$ and $P_{ij,sim}^2$ represent two-point correlation functions for phases i and j of the real sample and our simulated microstructure. Eq. (5) examines three independent two-point correlation functions of a real porous Ni–YSZ sample from scanning electron microscope (SEM) images and the corresponding functions of the reconstructed to have minimal differences. One example of the used SEM images is shown in Fig. 1. For the purpose of better illustration, the detected different phases are colored according to the color code used in Fig. 2 and Fig. 4.

For 2D and the subsequent 3D realizations, the following algorithm is pursued:

First of all, a fine 2D/3D grid is produced. In the cell generation step, nucleation sites on the grid can be randomly chosen or be selected based on the largest clusters of each phase in the SEM images of real samples. In both 2D and 3D reconstructions, the relative size of the nuclei of each phase corresponds to its volume fraction in the real sample. In the next step, the nuclei are redistributed by two consecutive operations: nuclei rotation and nuclei position change. The redistribution step is essential in fast convergence of the model and getting optimal results. Rotation about x, y and z axes (in case of 2D realization about x and y axes only) was accomplished by using the conventional Euclidean rotation matrices:
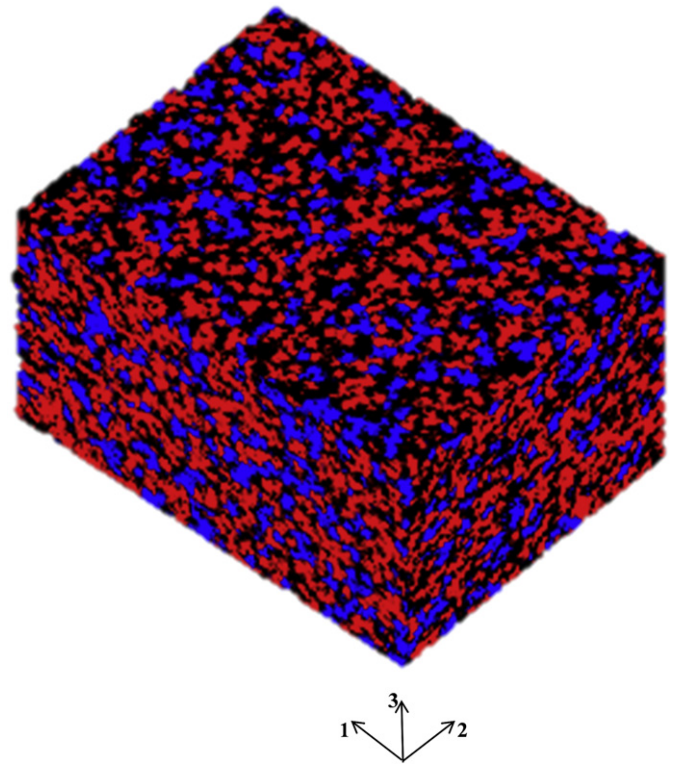

Fig. 2. The digital RVE. Red, blue and black represent YSZ, Ni and voids respectively. The length along axis 1 is 20.5 μm, along axis 2 is 15.4 μm and along axis 3 is 11.6 μm. (For interpretation of the references to color in this figure legend, the reader is referred to the web version of this article.)
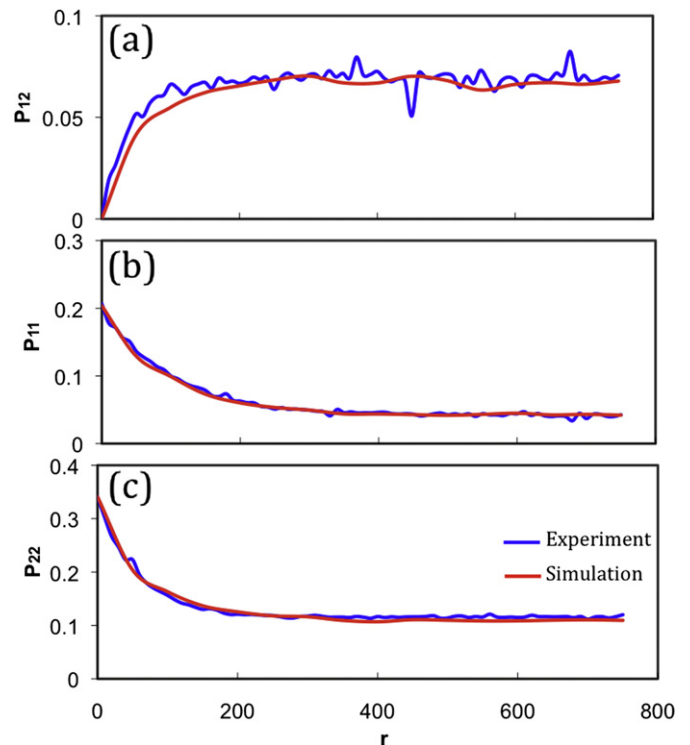

Fig. 3. Comparison of independent two point correlation functions of the digital and a real material. Phase 1 and 2 stand for Ni and void respectively.
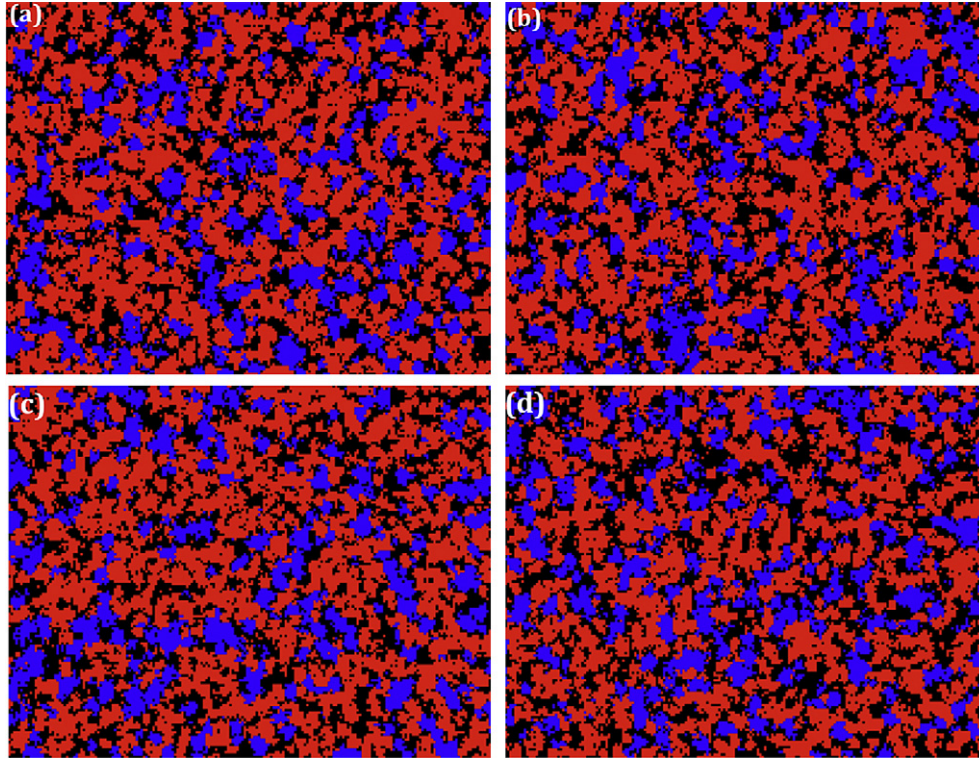
Fig. 4. Four 2D sections of the RVE at (a) 1 μm distance from origin along axis 3; (b) at 4.5 μm distance; (c) 8.5 μm and (d) 10.5 μm. Black, red and blue represent void, YSZ and Ni respectively. (For interpretation of the references to color in this figure legend, the reader is referred to the web version of this article.)

$$Q_x = \begin{bmatrix} 1 & 0 & 0 \\ 0 & \cos\theta_k & -\sin\theta_k \\ 0 & \sin\theta_k & \cos\theta_k \end{bmatrix}$$

$$Q_y = \begin{bmatrix} \cos\theta_k & 0 & -\sin\theta_k \\ 0 & 1 & 0 \\ \sin\theta_k & 0 & \cos\theta_k \end{bmatrix} \qquad (6)$$

$$Q_z = \begin{bmatrix} \cos\theta_k & -\sin\theta_k & 0 \\ \sin\theta_k & \cos\theta_k & 0 \\ 0 & 0 & 1 \end{bmatrix}$$

where

$$\theta_k = 2\pi\beta p_k \qquad (7)$$

$0 < \beta < 1$ is a random variable, and $0 \leq p_k \leq 1$ is an algorithm parameter factor. $k = 1,2,3,\ldots$ is an enumerator for algorithm parameter factors implying that different parameters should be used at different stages of the algorithm. After rotation, the positions of nuclei were changed using a simple polynomial function:

$$\boldsymbol{r} = L_e \beta p_k \qquad (8)$$

where $\boldsymbol{r}$ is the position vector of each nuclei and L_e is the length of the final microstructure in each x, y and z direction ($e = x, y, z$). The next part is changing the relative distance of the nuclei. Nuclei displacing was done based on the well-known colony algorithm [24] and is repeated until the following condition is satisfied:

$$\beta^n > \Omega \exp(\Omega v_i) \qquad (9)$$

where Ω and n are algorithm parameters.

The next step is growth of cells. Growth was accomplished by exploiting one of the natural growth algorithms seen in natural processes such as bacteria growth and insect colony aggregations. The algorithm is called cellular automaton [24] and acts based on the probability of adjacent cells possessing the same status as the current cell. In 2D reconstruction, 4 cells were considered as adjacent, while 6 cells were in 3D. Each redistributed nuclei is allowed to grow based on satisfaction of the following condition:

$$p_k > \beta \qquad (10)$$

If the condition in Eq. (10) is satisfied, and the cell is not occupied previously, growth toward the adjacent cell occurs.

In each run of the computer code, β and p_k values are kept constant. After each run which yields a realization of a 2D or 3D microstructure, the objective function (Eq. (5)) is calculated. Then, all the steps are repeated, and p_k values are altered until a minimized OF is obtained. The microstructure corresponding to the minimized OF is the final representative volume element (RVE) of the composite material which consists of aggregates of the three phases: Ni, YSZ and voids.

In the case of 3D realization, the 2D clusters are used as nuclei. To find their position in the 3D grid, the nuclei are extruded using a cubic shape function, $z = f(x,y) = \pm aK(i)$, where a and $K(i)$ are constants for each phase.

Fig. 2 demonstrates the reconstructed RVE of porous Ni–YSZ composite with $v_{Ni} = 0.2$, $v_{YSZ} = 0.45$ and, $v_{pore} = 0.35$ in accordance with volume fractions of a real sample with 8 mol% Y_2O_3. The computer code is capable of investigating percolation of each phase. The realized RVE is fully percolated for all the three phases. Therefore, such a composite in practice will show excellent electrical conductivity due to percolation of Ni and enhanced gas permeation as a result of void percolation. As a tradeoff, void percolation can significantly reduce mechanical properties [13].

2.2. Finite element simulations

Finite element method (FEM) was applied to homogenize the digital microstructure in order to reveal the temperature dependence of the desired properties. Percolation of Ni phase promises the necessary electrical conductivity. Other practically important properties include elastic response, thermal conductivity and thermal expansion coefficient. The studied temperature range starts from 25 °C and continues to 1000 °C in 100 °C intervals. VCAD™ software package was used to transfer the digital composite into a ~1.2 million irregular tetrahedral element mesh readable by Simulia ABAQUS™, which was the software package used to conduct finite element analyses. For obtaining results, the following assumptions were mandatorily made: (a) the microstructure does not change from increasing the temperature; meaning that sintering, grain growth and formation of new phases at higher temperatures were neglected. This assumption should not be a major source of error in simulations since all the aforementioned effects are negligible at working temperature range of real SOFC anode materials [2,3]. (b) Aggregates of Ni and YSZ in the RVE are mechanically and thermally isotropic meaning that the properties of aggregates in the RVE are the same along any direction. The polycrystalline nature of the aggregates in real samples matched the assumption fairly well. No assumption was made about anisotropy of the whole RVE. In addition, it was also assumed that (c) both Ni and YSZ behave linearly elastically and (d) the RVE remains perfectly bonded while applying mechanical loads.

The elastic response of the composite was fully investigated by means of performing three tensile and three shear tests at each temperature interval. The six total tests yield the 6 independent component of the stress tensor.

In all the tests, 1% deformation, either tensile or shear, was introduced to the RVE to develop corresponding stress (tensile or shear) and strain. At each test, all the components of strain and stress tensors were found by volume averaging over all the elements using the following equations:

$$\varepsilon_{ij} = \frac{1}{V_{\text{tot}}} \sum_{i=1}^{N} V_n \varepsilon_{ij}^n$$

$$\sigma_{ij} = \frac{1}{V_{\text{tot}}} \sum_{i=1}^{N} V_n \sigma_{ij}^n \qquad (11)$$

where ε_{ij} and σ_{ij} are components of the strain and stress tensor respectively. The superscript n denotes the strain or stress component in the nth element. V_{tot} is the total volume of the RVE and V_n is the volume of the nth element. N is the total number of elements. Knowing all the components of strain and stress tensor at each temperature interval, finding the components of compliance tensor is straightforward.

$$\varepsilon_{ij} = S_{ijkl}\sigma_{kl} \qquad (12a)$$

The two independent temperature dependent elastic parameters of pure Ni and 8YSZ have been experimentally measured and reported elsewhere [25,26].

Thermal conductivity (TC) was computed along the three mutually perpendicular directions of the RVE. At each temperature T, a temperature difference equal to $T - T_0$ was introduced to the RVE along each direction. T_0 is a reference temperature and for simplicity was chosen as 0 °C in all the simulations. Similar to the elastic case, the volume average of temperature gradient component and heat flux vector component along the desired direction was assessed using the following equation:

$$\kappa_i = \frac{1}{V_{\text{tot}}} \left(\sum_{n=1}^{N} V_n q_i^n \middle/ \sum_{n=1}^{N} V_n \frac{\partial T^n}{\partial x_i} \right) \qquad (12b)$$

where κ_i is the TC coefficient along i (i = 1, 2 or 3). q_i^n is the heat flux vector component along i in element n. $\partial T^n/\partial x_i$ is the component of temperature gradient vector in element n along direction i. The rest of symbols have their regular meanings.

The thermal expansion coefficient (TEC) of the material was calculated by measuring the volume average thermal strain developed in each direction when the temperature difference $T - T_0$ was introduced. Eq. (13) further clarifies the calculations:

$$\alpha_i = \frac{1}{V_{\text{tot}}} \left(\sum_{n=1}^{N} V_n \varepsilon_{ii,th}^n / T - T_0 \right) \qquad (13)$$

where α_i is the TEC along i and $\varepsilon_{ii,th}^n$ is the thermal strain component in ith direction in the nth element. The rest of symbols have their regular meanings. In finite element simulations, the previously reported experimental values of specific heat, thermal expansion coefficient, thermal conductivity of Ni, 8YSZ and void (air, in case of thermal properties) were used [27–30].

3. Results and discussion

3.1. Microstructural aspects

The novel model of 3D reconstruction successfully converged to build a relatively large RVE of porous Ni–YSZ composite (Fig. 2). The lengths along the 1, 2 and 3 axes are 20.5, 15.4 and 11.6 μm respectively. The independent two point correlation functions for the real and reconstructed microstructure are shown in Fig. 3. There is a decent coincidence of the curves in all the cases implying the prominent fact that the reconstructed RVE is sufficiently statistically equivalent to the real material. Although a complete equivalence of a digital microstructure to a real sample needs more analyses of other morphological and geometrical factors, similarity in two-point correlation functions and subsequent assumption of similar properties is usually considered an acceptable measure [17,20,22,31–33]. Fig. 4 illustrates four 2D sections of the 3D composite at different positions along axis 3. These 2D sections illustrate that the material is completely random in the interior of the composite and there is no gradient in average aggregate sizes of any phase.

3.2. Elastic properties

The full 21-component compliance tensor at room temperature is as follows:

$$S\left((\text{GPa})^{-1}\right) = \begin{bmatrix} 0.058613 & -0.016284 & -0.016988 & 2.63 \times 10^{-4} & -2.71 \times 10^{-4} & -5.73 \times 10^{-5} \\ & 0.05755 & -0.01664 & 2.11 \times 10^{-4} & -1.78 \times 10^{-4} & -2.78 \times 10^{-4} \\ & & 0.05653 & -9.08 \times 10^{-5} & -1.82 \times 10^{-4} & -6.06 \times 10^{-5} \\ & & & 0.21 & 1.23 \times 10^{-5} & -8.04 \times 10^{-7} \\ & & & & 0.155 & 3.82 \times 10^{-5} \\ & & & & & 0.155 \end{bmatrix}$$
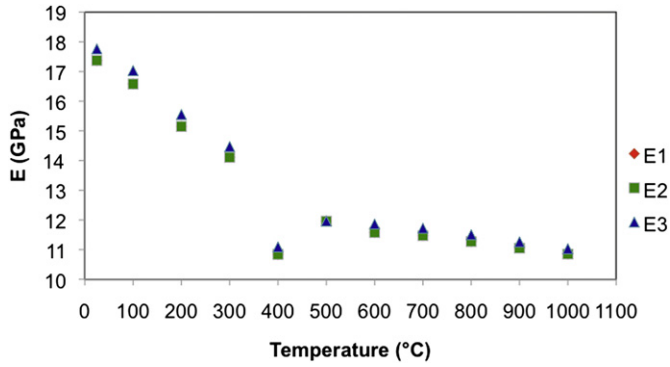
Fig. 5. Temperature dependence of effective elastic moduli of the digital RVE at three mutually orthogonal axes. E_1 and E_2 fully overlap.

Fig. 7. Temperature behavior of lateral strain coefficients (Poisson's ratios) vs. temperature.

The components shown by scientific numbers (all the off diagonal components in the right half of the matrix) are at least two orders of magnitude smaller than the other components. For the sake of conciseness and practical usefulness of the results, we assume that these values are zero in the compliance tensor. Therefore the general compliance tensor at any temperature would have following form:

$$ S = \begin{bmatrix} \dfrac{1}{E_1} & -\dfrac{\nu_{12}}{E_2} & -\dfrac{\nu_{13}}{E_3} & 0 & 0 & 0 \\[2mm] -\dfrac{\nu_{21}}{E_1} & \dfrac{1}{E_2} & -\dfrac{\nu_{23}}{E_3} & 0 & 0 & 0 \\[2mm] -\dfrac{\nu_{31}}{E_1} & -\dfrac{\nu_{32}}{E_2} & \dfrac{1}{E_3} & 0 & 0 & 0 \\[2mm] 0 & 0 & 0 & \dfrac{1}{G_1} & 0 & 0 \\[2mm] 0 & 0 & 0 & 0 & \dfrac{1}{G_2} & 0 \\[2mm] 0 & 0 & 0 & 0 & 0 & \dfrac{1}{G_3} \end{bmatrix} \qquad (14) $$

This is the elastic response of an orthotropic material. The ν_{ij} and E_i values are correlated to each other:

$$ \frac{\nu_{ij}}{E_j} = \frac{\nu_{ji}}{E_i} \qquad (15) $$

Thus, orthotropic materials possess 9 independent components, i.e. a type of material between the two extremes cases: fully anisotropic 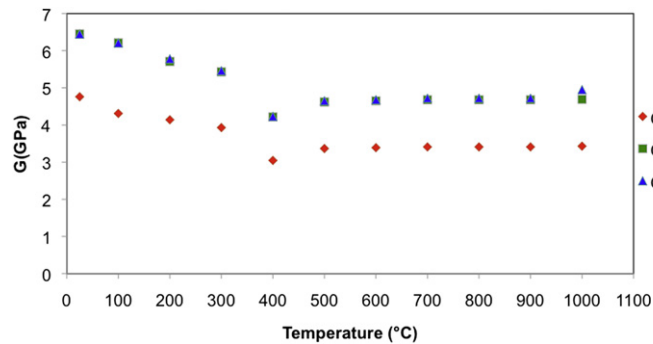and fully isotropic. With the assumption that the RVE can be fairly described by the orthotropic behavior, the components of the compliance tensor are evaluated.

Fig. 5 shows the temperature dependence of E_i moduli. The room temperature values are close to 18 GPa which is in the order of the widely scattered values reported for real porous Ni–YSZ samples with 35% void in the microstructure [13,14].

E_1 and E_2 are different from each other by at most 2%, while the values of E_3 are slightly higher than the other two with at most a 4% difference. Fig. 6 exhibits the trend in change of G_i moduli vs. temperature. The values start around 8 GPa at room temperature and reduce down to 5 GPa. Compared to E_i, shear moduli behavior of the digital material along the axes is different. In case of shear, the different value is G_1 being lower than G_2 and G_3 by an average of ∼20%. This reflects the contrast in shear and tension moduli of the digital composite.

The independent ν_{ij} components against temperature are plotted in Fig. 7. The average room temperature value is 0.285 which decreases to ∼0.23 at 1000 °C. It suggests that effects of lateral strains are smaller at higher temperatures compared to room temperature. This is a useful point in design of the fuel cells since the anode and electrolyte needs to be in contact during service. Lateral strains can deteriorate the contact and should be considered in design.

3.3. Thermal conductivity and thermal expansion

Fig. 8 shows TC coefficients along the three orthogonal axes. The room temperature values of the reconstructed material are ∼28 W mK^{-1} which are in the range of experimentally reported values [16]. TC of the digital composite decreases by increasing T until ∼500 °C after which it slightly increases/remains constant. TC
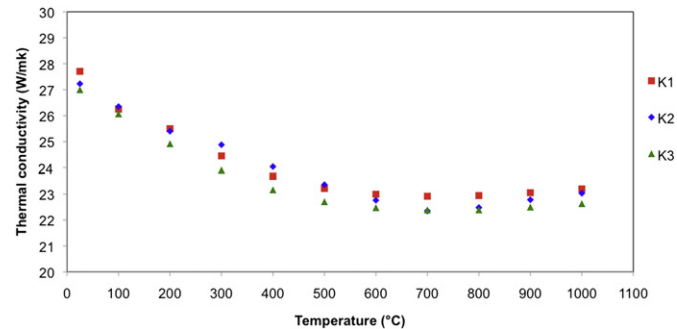

Fig. 6. Temperature dependence of shear moduli of the digital RVE. G_2 and G_3 fully overlap.

Fig. 8. Changes of thermal conductivity coefficients as a function of temperature in the digital RVE along three orthogonal axes.
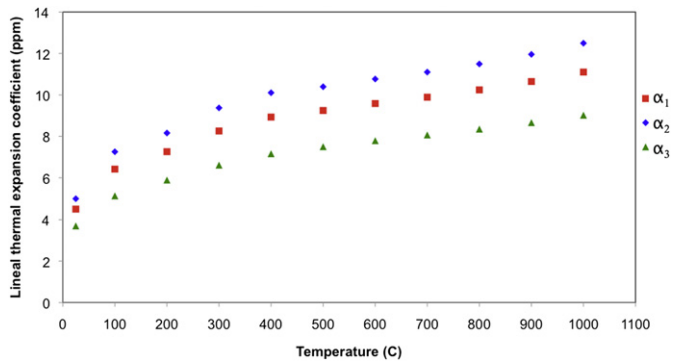
Fig. 9. Thermal expansion coefficient of the RVE vs. temperature along three orthogonal axes.

of pure Ni follows the same temperature-dependence trend [29] suggesting that Ni controls TC behavior in the digital RVE. This is a clear evidence for the percolation of Ni phase that also guarantees the excellent electrical conductivity if a composite with this microstructure is used in practice. Closeness in three κ_i values at all temperatures implies isotropy in TC response of the microstructure.

Fig. 9 exhibits TEC of the RVE vs. temperature. There is a constant increase from the average $\sim 4 \times 10^{-6}$ at room temperature to an average of $\sim 10.2 \times 10^{-6}$ at 1000 °C. Computed TECs are in the range of experimentally measured values for porous Ni–YSZ composites [16,17]. TEC values of the RVE at higher temperatures are distributed at farther distances compared to room temperature implying an increase in anisotropy of thermal expansion as temperature increases. At temperatures above 800 °C, the difference between TEC of the digital composite and the electrolyte (YSZ) [27] gets above 50% which can, in practice, lead to failure of the device.

4. Conclusions

In this work, a digital 3D microstructure of a porous Ni–YSZ composite was successfully realized using a recently developed Monte Carlo technique. By a direct comparison of the two-point correlation functions between the realized material and a real composite, the "sufficient" statistical equivalency was verified. A finite element method was applied to study elastic behavior, thermal conductivity and thermal expansion characteristics of the realized material as functions of temperature. All the computed room temperature properties of the material are in the order of experimentally reported values. It suggests that at higher temperatures, where a full set of experimental values is not available, the computed properties follow the same trend as in room temperature and are very close to the properties of the real materials. It is observed that in elastic domain, the digital material is not fully anisotropic and shows a behavior similar to orthotropic materials. In addition, the trends in shear and tensile behaviors are not the same. However, in thermal conductivity of the same realized sample, responses are in a manner very close to the fully isotropic type. Furthermore, there are indications of the fact that thermal conductivity behavior of the digital material is mostly controlled by the Ni phase. In thermal expansion, the anisotropy increases by increasing the temperature which contributes to the failure of the material as a result of thermal strains.

Acknowledgments

References

[1] K. Kendall, Nature Materials 1 (2002) 211–212.
[2] X. Zhang, S.H. Chan, G. Li, H.K. Ho, J. Li, Z. Feng, Journal of Power Sources 195 (2010) 685–702.
[3] A.B. Stambouli, E. Traversa, Renewable and Sustainable Energy Reviews 6 (2002) 433–455.
[4] M.A. Laguna-Bercero, Journal of Power Sources 203 (2012) 4–16.
[5] M. Lankin, Y. Du, C. Finnerty, Journal of Fuel Cell Science and Technology 8 (2011) 054001.
[6] S. Chen, Y. Chen, H. Finklea, X. Song, G. Hackett, K. Gerdes, Solid State Ionics 206 (2012) 104–111.
[7] O. Yamamoto, Electrochimica Acta 45 (2000) 2423–2435.
[8] B. Steele, A. Heinzel, Nature 414 (2001) 345–352.
[9] W. Zhu, S. Deevi, Materials Science and Engineering A 362 (2003) 228–239.
[10] O. Costa-Nunes, R. Gorte, J. Vohs, Journal of Power Sources 141 (2005) 241–249.
[11] H. Koide, Y. Someya, T. Yoshida, T. Maruyama, Solid State Ionics 132 (2000) 253–260.
[12] J. Kong, K. Sun, D. Zhou, N. Zhang, J. Mu, J. Qiao, Journal of Power Sources 166 (2007) 337–342.
[13] J. Yu, G. Park, S. Lee, S. Woo, Journal of Power Sources 163 (2007) 926–932.
[14] M. Pihlatie, A. Kaiser, M. Mogensen, Journal of the European Ceramic Society 29 (2009) 1657–1664.
[15] J. Roa, M. Laguna-Bercero, A. Larrea, V. Orera, M. Segarra, Ceramics International 37 (2011) 3123–3131.
[16] T. Kawashima, M. Hishinuma, Materials Transactions JIM 37 (9) (1996) 1518–1524.
[17] J. Johnson, J. Qu, Journal of Power Sources 181 (2008) 85–92.
[18] J. Wilson, W. Kobsiriphat, R. Mendoza, H. Che, J. Hiller, D. Miller, K. Thornton, P. Voorhees, S. Adler-Scott, A. Barnett, Nature Materials 5 (2006) 541–544.
[19] M. Li, T. Xu, Progress in Materials Science 56 (2011) 864–899.
[20] M. Baniassadi, H. Garmestani, D.S. Li, S. Ahzi, M. Khaleel, X. Sun, Acta Materialia 59 (2011) 30–43.
[21] H. Garmestani, M. Baniassadi, D.S. Li, M. Fathi, S. Ahzi, International Journal of Theoretical and Applied Multiscale Mechanics 1 (2009) 134–149.
[22] S. Torquato, Random Heterogeneous Materials, Springer, New York, 2001.
[23] P. Debye, Annals of Physics 46 (1915) 809.
[24] A. Ilachinsk, Cellular Automata, World Scientific, , Singapore, 2001.
[25] R. Farrarao, R. McLellan, Metallurgical and Materials Transactions A 8 (1977) 1563–1565.
[26] S. Giraud, J. Canel, Journal of European Ceramic Society 28 (2008) 77–83.
[27] X. Song, M. Xie, f. Zhou, G. Jia, X. Hao, S. An, Journal of Rare Earths 29 (2011) 155–159.
[28] T. Kollie, Physical Review B 16 (11) (1977) 4872–4881.
[29] P. Desai, International Journal of Thermophysics 8 (1987) 763–780.
[30] H. Hayashi, T. Saitou, N. Maruyama, H. Inaba, K. Kawamura, M. Mori, Solid State Ionics 176 (5–6) (2005) 613–619.
[31] M.C. Rechtsman, S. Torquato, Journal of Applied Physics 103 (8) (2008) 084901–084901-15.
[32] Y. Jiao, F. Stillinger, S. Torquato, Physical Review E 77 (3) (2008) 031135.
[33] D. Pham, S. Torquato, Journal of Applied Physics 94 (10) (2003) 6591–6602.